PCCP

Ultrafast dynamics in LMCT and intraconfigurational excited states in hexahaloiridates(IV), models for heavy transition metal complexes and building blocks of quantum correlated materials

Journal:	*Physical Chemistry Chemical Physics*
Manuscript ID	CP-ART-01-2020-000438.R2
Article Type:	Paper
Date Submitted by the Author:	16-Jun-2020
Complete List of Authors:	Budkina, Darya; Bowling Green State University, Department of Chemistry, Center for Photochemical Sciences Gemeda, Firew ; Bowling Green State University, Department of Chemistry Matveev, Sergey; University of Illinois at Urbana-Champaign, Department of Chemistry Tarnovsky, Alexander; Bowling Green State University, Department of Chemistry

ARTICLE

Ultrafast dynamics in LMCT and intraconfigurational excited states in hexahaloiridates(IV), models for heavy transition metal complexes and building blocks of quantum correlated materials

Received 00th January 20xx,
Accepted 00th January 20xx

DOI: 10.1039/x0xx00000x

Darya S. Budkina, [a,b] Firew T. Gemeda, [a] Sergey M. Matveev, [a,c] and Alexander N. Tarnovsky[a†]

The population and structural dynamics of $IrCl_6^{2-}$ is studied in acetonitrile and aqueous solutions in comparison to isoelectronic $IrBr_6^{2-}$ using ultrafast broadband, dispersed transient absorption, with both octahedra excited with 85 fs pulses at four different wavelenths, encompassing the first seven t_{2g}-based electronic states. Ligand-to-metal charge transfer (LMCT) 420- or 490-nm excitation of $IrCl_6^{2-}$ into $U_u'(^2T_{2u})$ + $E_u''(^2T_{2u})$ states, superimposed due to Ham effect, or $U_u'(^2T_{1u})$, respectively, leads to symmetry lowering due to Jahn-Teller effect in these excited states with the subsequent 100-fs decay into $U_g'(^2T_{1g})$. This first LMCT state is formed vibrationally coherent in the 104 cm^{-1} t_{2g} (scissor) or 243 cm^{-1} e_g (out-of-phase-stretch) Jahn-Teller modes for the respective excitation wavelength. Direct excitation into $U_g'(^2T_{1g})$ at 600 nm and the intraconfigurational lowest excited $U_g'(^2T_{2g})$ state at 1900 nm helped to establish that $U_g'(^2T_{1g})$ decays via back electron transfer into $U_g'(^2T_{2g})$ (time constants, 3.55 ps in acetonitrile and 0.9 ps in water), and the decay of $U_g'(^2T_{2g})$ into the ground state is the rate-limiting relaxation step. The relaxation cascade of $IrBr_6^{2-}$ is similar with short-lived (≤ 100 fs) higher LMCT states, but the vibrational coherence is only observed in the Jahn-Teller t_{2g} mode. Faster back electron transfer for $IrBr_6^{2-}$ is explained by the energy gap law. The intraconfigurational $U_g'(^2T_{2g})$ states, which are ~5100 cm^{-1} above the ground state for both complexes, have a sub-nanosecond lifetime largely independent of the ligand nature (~350 ps, acetonitrile).

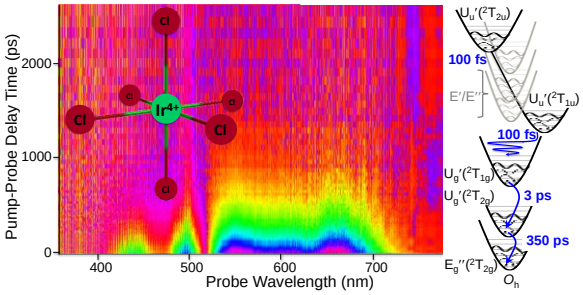

1. Introduction

Excited electronic states in transition metal compounds have found ubiquitous use in modern science and technology.[1,2] The low-spin, heavy transition metal compounds drawn from Os and Ir in the Os^{3+} and Ir^{4+} oxidation states (the 5*d* series) uniquely have a manifold of excited states that starts at energies as low as a fraction of eV and the different nature of which can be linked to specific applications. These compounds have attracted attention in up-conversion and photocatalysis[3-8] as well as physics (magnetism and high-temperature superconductivity) of strongly correlated materials,[9,10] where they serve as building blocks. The above phenomena are governed by the compound's excited-state electronic structure, where two effects are central: Jahn-Teller (JT) coupling of the electronic and nuclear motion[11-13] and spin-orbit coupling (SOC) that entangles the orbital and spin angular momenta of electrons.[14] Strong SOC effectively reduces the orbital degeneracy, leading to novel quantum materials with unique metal-insulator transitions and magnetic properties.[9,10] In the JT effect, a non-linear molecule in an orbitally degenerate electronic state spontaneously distorts enabling energy and charge localization, which may be utilized in light-powered molecular machines. Mixing of spin, electronic, and nuclear degrees of freedom leads to competing SOC and JT interactions[15] and rather complex spin-vibronic dynamics.[16,17]

Excited states of Ir(IV) hexahalides have been extensively interpreted starting from pioneering studies of solution spectra[18,19] followed by high-resolution optical and magnetic circular dichroism (MCD) work in solids.[20-33] $IrCl_6^{2-}$ is the most industrially important precursor iridium compound.[34] Ultrafast excited-state dynamics of a low-spin $5d^5$ $IrCl_6^{2-}$ complex and its comparison to isoelectronic $IrBr_6^{2-}$ is the focus of the present study. Both complexes in the condensed phases, on symmetry ground, retain octahedral (O_h) symmetry in the electronic

[a] Center for Photochemical Sciences, Department of Chemistry, Bowling Green State University, Bowling Green, Ohio, USA.
[b] Present address: School of Chemistry and Biochemistry, University of Geneva, 1211 Geneva 4, Switzerland
[c] Present address: Department of Chemistry, University of Illinois at Urbana-Champaign, Champaign–Urbana, Illinois 61801, USA
† E-mail: atarnov@bgsu.edu.

Electronic Supplementary Information (ESI) available: steady-state absorption spectra of $IrCl_6^{2-}$ and rBr_6^{2-}, spectral assignments and short-time transient absorption spectra of $IrCl_6^{2-}$ and neat solvents, transient absorption kinetic traces and global fits for $IrCl_6^{2-}$, and results of the FFT analysis of vibrational coherences of excited $IrCl_6^{2-}$ and $IrBr_6^{2-}$, all above in acetonitrile and water. See DOI: 10.1039/x0xx00000x

ground state[21,27,35-41] (Kramers twofold degeneracy[12]), and are isoelectronic to predominantly O_h perovskite iridates.[9,10,42] In the O_h ligand-field (LF), five d-orbitals of Ir(IV) are split into three t_{2g} and two e_g type orbitals. Metal SOC causes further splitting of t_{2g} into doubly degenerate $u_g'(t_{2g})$ and a higher $e_g''(t_{2g})$ metal orbitals separated by $3/2\zeta_M$,[43-45] where ζ_M is the metal spin-orbit parameter (~3600 cm^{-1} for iridium[22,28,45-49]). The $u_g'(t_{2g})$ and $e_g''(t_{2g})$ metal orbitals primarily contribute to $u_g'(t_{2g})$ and $e_g''(t_{2g})$ molecular orbitals, a picture which is also supported by the relativistic calculations.[46-49] The upper (singly-occupied) spin component is the destination for the visible ligand-to-metal charge-transfer (LMCT) and short-wave-infrared intraconfigurational (that is within the t_{2g} multiplet) transitions. The LF e_g orbital is not involved as it is at higher energies ($10Dq$ ~ 3.3 eV). Studies of $IrCl_6^{2-}$ and similar ions in low-temperature rigid media gave evidence for excited-state JT effects through the anomalies in the stationary spectra,[20,22,31,50,51] in addition to SOC effects. $IrCl_6^{2-}$ and $IrBr_6^{2-}$ are also isoelectronic to low-spin $Fe(CN)_6^{3-}$, which is a model for studies of solution-phase LMCT excitations[52,53] for which few systematic ultrafast spectroscopic investigations exist, in contrast to MLCT. In $Fe(CN)_6^{3-}$, the ζ_M parameter and, therefore, the t_{2g} splitting is much smaller.[45,54] Studies of Ir(IV) hexahalides can enhance our understanding of LMCT reactions with large relativistic effects.

Upon irradiation in the gas phase, $IrCl_6^{2-}$ and $IrBr_6^{2-}$ fragment into polyatomic and atomic halide anions.[55-58] Femtosecond time-resolved photoelectron spectroscopy work[59] suggested that $IrBr_6^{2-}$ excited into the third LMCT state (760 nm) undergoes rapid cascade relaxation into the hot ground state, where a delayed unimolecular fragmentation (a 79 ps time constant) takes place. Such photochemistry is not expected in solution where the solvent rapidly dissipates solute's excess vibrational energy. Early solution studies showed that UV irradiation of both hexahaloiridates form photoaquated products.[60,61] $IrCl_6^{2-}$ and $IrBr_6^{2-}$ are substitution inert upon visible irradiation (in particular, in the 420-495 nm range for the chloride in water),[60-62] in contrast to analogous d^6 complexes ($PtCl_6^{2-}$ and $PtBr_6^{2-}$ [63]). Recent ultrafast transient absorption studies also reported no photosubstitution upon excitation as high as the 6th LMCT state for $IrBr_6^{2-}$ (525 nm[64]) and $IrCl_6^{2-}$ (400-420 nm[65,66]). In the last case, ground-state $IrCl_6^{2-}$ recovered with a time constant of 18 ps in aqueous solutions and ~30 ps in methanol and ethanol, but neither the role of the intermediate excited states nor the solvent in the radiationless relaxation mechanism was clear.[65-67] For the short-wave-infrared intraconfigurational state of $IrBr_6^{2-}$, an unexpectedly slow decay in acetonitrile and chloroform (~350 ps time constants[64,68]) and a much faster decay in aqueous solutions due to energy transfer involving the OH group were reported.[64] The 100-fs LMCT lifetimes and vibrational coherences observed for $IrBr_6^{2-}$ indicate the importance of excited-state JT effect in driving the relaxation dynamics.[64] This conclusion is in contrast to the recent femtosecond 2D electronic spectroscopy study of $IrBr_6^{2-}$, where the LMCT decay was suggested to be driven by SOC alone.[35]

In this work, broadband, dispersed transient absorption spectra were measured following 85-fs excitation of $IrCl_6^{2-}$ into excited states of various types (one intraconfigurational and three LMCT) in water and acetonitrile. We portray the radiationless relaxation mechanism and provide an accurate assessment of the role of the first seven excited states. The relaxation dynamics is compared to that of isoelectronic, low-spin d^5 $IrBr_6^{2-}$. The findings can serve as a platform for wider discussion of heavy transition metal compounds where spin-orbit interactions are comparable to or larger than vibronic interactions. The results emphasize the importance of symmetry-induced JT intersections as a driving force for the ultrafast relaxation dynamics even in molecular systems with very significant spin-orbit interactions.

2. Experimental

2.1 Materials

Deionized water (Nanopure) and anhydrous acetonitrile (HPLC ≥ 99.9%, Sigma-Aldrich), which was prepared according to standard methods, were used as solvents. K_2IrCl_6 and K_2IrBr_6 (Surepure Chemetals) were used to prepare aqueous solutions. To be soluble in acetonitrile potassium cations were substituted by tetrabutylammonium cations (tBu$_4$NCl and tBu$_4$NBr were used, Sigma-Aldrich). The substitution reaction was carried out in aqueous solutions where K_2IrCl_6 and K_2IrBr_6 are soluble, whereas $(t\text{Bu}_4\text{N})_2IrCl_6$ and $(t\text{Bu}_4\text{N})_2IrBr_6$ are not. Precipitate was washed with cooled ethanol (HPLC ≥ 99.9%) to eliminate traces of water and then dried under vacuum. All chemicals were used as received.

2.2 Methods

Near-IR (800-2900 nm, only in CH_3CN) and UV-vis absorption spectra of solutions were measured in Infrasil and Spectrosil quartz cells using a PerkinElmer LAMBDA 750 and a Varian Cary 50 Bio spectrophotometer, respectively. In the transient absorption set-up used,[69,70] the 50% part of the output of a Ti:Sa amplified laser system (800 nm, 85 fs, 0.9 mJ $pulse^{-1}$, and 1 kHz) was split and sent to a TOPAS optical parametric amplifier to generate 420, 490, 600 nm (7 μJ $pulse^{-1}$) and 1900 nm (11 μJ $pulse^{-1}$) excitation pulses, which were then chopped at 500 Hz. The excitation light was sent through a Berek compensator to set the polarization plane to the magic angle (54.7°) with respect to that of the probe light, and focused onto the sample (solution in a 2-mm pathlength spinning cell). For 420- and 490-nm excitation, the $IrCl_6^{2-}$ concentration was 0.9 mM in H_2O and 0.5 mM in CH_3CN. For 1900- and 600-nm excitation, 1.7 mM solutions were used. The same concentration of $IrBr_6^{2-}$ was used for 602-nm excitation. The remaining 50% portion of the amplified output was attenuated and focused onto a 4-mm thick CaF_2 window to generate a broadband (340-780 nm) white light continuum, which was then split into a probe and a reference beam. The reference beam bypassed the sample and the probe beam was made to overlap the excitation beam at the sample position at a 6°- angle, with the excitation and probe beam diameters being 200 and 60 μm. Afterwards, the probe and reference beams were dispersed by a spectrograph, and the corresponding light was recorded in a 274 nm window using

two diode arrays read out at 1 kHz for derivation of transient absorption (ΔA) signals. The dependence of the ΔA signals with excitation energy was linear and passed through the origin. The excitation pulse energies used are specified in the text.

All ΔA data were corrected for group-velocity dispersion in the probe light with a 25-fs accuracy using the solvent cross-phase modulation and stimulated Raman scattering signals centered at a time zero.[71,72] Using these signals, the width of the cross-correlation function (CCF) between the excitation and probe pulses is evaluated to be 100 fs (fwhm, Gaussian shaped). The neat solvent ΔA signals persisted for the initial ~100 fs, but were smaller than the corresponding ΔA signals measured for $IrCl_6^{2-}$ and $IrBr_6^{2-}$ solutions under the same excitation conditions. The cell front window had only a minor contribution to these signals. This allowed accurate subtraction of the solvent signals from the solution signals (after proper scaling of the former to account for solute absorption at the excitation wavelength). To describe the dynamics, global fit analysis was carried out where recorded ΔA kinetic traces, excluding the initial 75 fs, were simultaneously fitted to a sum of exponents $\sum_j a_j(\lambda)e^{-t/\tau_j}$, where τ_j is the j-time constant and $a_j(\lambda)$ is the decay-associated difference spectrum evolving with τ_j. From the $a_j(\lambda)$ spectra, assuming the consecutive relaxation mechanisms, the evolution-associated difference spectra ($\varepsilon_j(\lambda)$ or EADS, see p. 97[73]) were reconstructed. The $\varepsilon_j(\lambda)$ rises with a τ_{j-1} time constant. The global fit assumes that line shapes do not change with time, which can affect τ_j values on a time scale of vibrational relaxation, typically several picoseconds in solution. Multiexponential fits with CCF deconvolution were also performed at several representative probe wavelengths. Fit residuals $R(\lambda, t)$ were analyzed using fast Fourier transform (FFT).

3. Results

3.1 Steady-state absorption spectra

In the visible region (> 350 nm), $IrCl_6^{2-}$ in acetonitrile has two strong absorption bands peaking at 437 and 492 nm (ε = 3110 and 3400 M^{-1} cm^{-1}, respectively) and a weaker 586-nm band (ε = 230 M^{-1} cm^{-1}), Fig. 1. Also, there is another, much weaker 1900-nm band (ε ~ 65 M^{-1} cm^{-1}), which is the lowest-energy absorption transition of $IrCl_6^{2-}$ as well as $IrBr_6^{2-}$, Fig. S1 of ESI. The absorption spectra in aqueous solutions are similar, but they are broadened and somewhat blue-shifted, consistent with the previous studies.[58,74] The shift is ~730 cm^{-1} for 437-nm band of $IrCl_6^{2-}$ (~600 cm^{-1}, 535-nm band of $IrBr_6^{2-}$ [64]), but much less for other visible bands. Greater stabilization of the ground in comparison to the LMCT states in a more polar solvent explains the shift direction.[56] Both complexes exhibit significant thermal and photostability in acetonitrile. Special care including usage of fresh solutions and limited exposure times was taken for aqueous solutions in which hexahaloiridates are less stable in dark.[75,76]

3.2 Spectral assignments and the electronic structure of $IrCl_6^{2-}$.

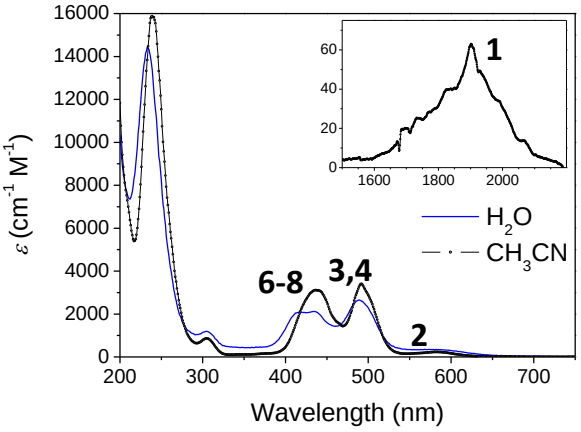

Fig. 1. Molecular decadic extinction coefficient (ε) spectra of $IrCl_6^{2-}$ in acetonitrile and water. The inset shows the near-IR absorption band of $IrCl_6^{2-}$ in acetonitrile due to the $E_g'' \rightarrow U_g'$ intraconfigurational transition. Electronic transitions of the complex are numbered 1-8 for spectral assignments, see Table 1.

We assigned the absorption bands of $IrCl_6^{2-}$ in solution based on previous spectroscopic studies of $IrCl_6^{2-}$ in low- and room-temperature solids. Table 1 summarizes the assignments made for $IrBr_6^{2-}$ [64] and $IrCl_6^{2-}$. Metal SOC splits the $^2T_{2g}(t_{2g}^5)$ term into the ground $E_g''(^2T_{2g})$ and first excited $U_g'(^2T_{2g})$ states, Fig. 2. The lowest energy $E_g'' \rightarrow U_g'$ transition is intraconfigurational, corresponding to electron promotion from the u_g' to the e_g'' within the t_{2g} manifold. As seen in Fig. 1 and Fig. S1 of ESI, the $E_g'' \rightarrow U_g'$ transition energy in solution agrees with that in room-temperature solids[28] (~5000 cm^{-1}). The $E_g'' \rightarrow U_g'$ transition is La-Porte forbidden,[77] but the prohibition is partially lifted through vibronic coupling to odd parity vibrational modes (t_{2u}, t_{1u}).[25,26] All other $IrCl_6^{2-}$ transitions above 350 nm (above 500 nm, $IrBr_6^{2-}$) are due to electron transfer to the $e_g''(t_{2g})$ orbital from various ligand orbitals, in order of decreasing energy: π t_{1g}, (π + σ) t_{1u}, and π t_{2u} (π t_{2g} lies lower[22,78] than π t_{2u}). SOC splits

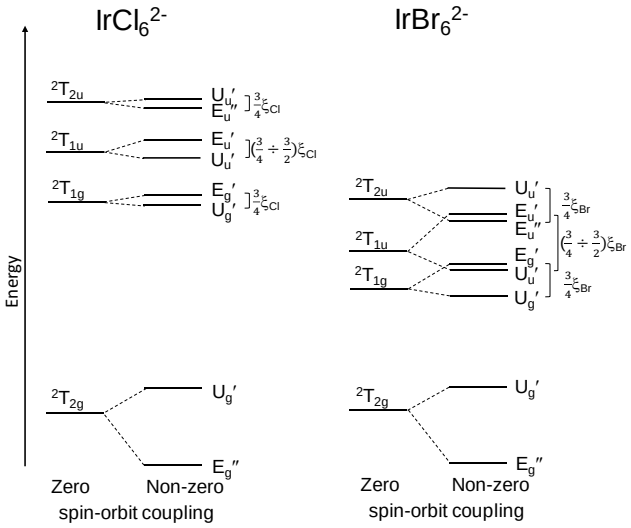

Fig. 2. Energy level diagram of ground-state $IrCl_6^{2-}$ and $IrBr_6^{2-}$ accounting for SOC as modeled by Schatz,[22] taking into account spin-orbit coupling. Lande spin-orbit coupling parameters: ξ_{Ir} = 3600 cm^{-1}, ξ_{Cl} = 587 cm^{-1}, and ξ_{Br} = 2457 cm^{-1}.[20] Energies of T-levels in the absence of spin-orbit coupling are shown only as the guidance.

Table 1 Electronic transitions and their assignments for $IrCl_6^{2-}$ (λ > 350 nm) and $IrBr_6^{2-}$ (λ > 500 nm) in acetonitrile.[a] The transition numbering corresponds to Fig. 1.[b] Electronic configurations of the ground and excited states are given in Griffith notation.[14]

N	$IrCl_6^{2-}$ $\bar{\nu}$, cm^{-1} (λ, nm)	$IrBr_6^{2-}$ $\bar{\nu}$, cm^{-1} (λ, nm)	Assignments [e]	Type
1	5258 (1902)	4938 (2025)	$E_g''(^2T_{2g}) \rightarrow U_g'(^2T_{2g})$	*d-d*
2	17065 (586)	11351 (881)	$E_g''(^2T_{2g}) \rightarrow U_g'(^2T_{1g})$	LMCT Ligand($X^{c)}$) to t_{2g}(Ir)
3	20325 (492)	13333 (750)	$E_g''(^2T_{2g}) \rightarrow U_u'(^2T_{1u})$	
4		14045 (712)	$E_g''(^2T_{2g}) \rightarrow U_u'(^2T_{1u})$	
5	[d]	14577 (686)	$E_g^{2}''(T_{2g}) \rightarrow E_g'(^2T_{1g})$	
6	22989 (435)	16667 (600)	$E_g''(^2T_{2g}) \rightarrow E_u''(^2T_{2u})$	
7		18116 (552)	$E_g''(^2T_{2g}) \rightarrow U_u'(^2T_{2u})$	
8		18692 (535)	$E_g''(^2T_{2g}) \rightarrow U_u'(^2T_{2u})$	

[a] Because absorption spectra of $IrCl_6^{2-}$ and $IrBr_6^{2-}$ in acetonitrile and water are similar, but the bands are narrower in acetonitrile, we base our spectral assignments on the spectra in acetonitrile. [b] See Fig. S1, ESI for the steady-state absorption spectrum of $IrBr_6^{2-}$. [c] X=Cl or Br [d] Observed at 18650 cm^{-1} (536 nm) in doped crystals, ref. [22] [e] Assignments for $IrBr_6^{2-}$ follows ref. [64].

the ligand orbitals as shown in Fig. 2, with the splittings proportional to a ligand spin-orbit constant; ζ_{Br} = 2457 cm^{-1} and ζ_{Cl} =587 cm^{-1}.[20] Consequently, the T_{1g}, T_{1u}, and T_{2u} terms split into U' and E'(E") LMCT states. The less intense and broad 586-nm $U_g'(^2T_{1g})$ band corresponds to a parity-forbidden transition originating from the t_{1g}. This band in doped crystals[22,31] shows a small contribution from the $E_g'(^2T_{1g})$ component (doubly forbidden based on the parity and total momentum in the j-j coupling scheme).[31] Two strong bands at 23000 and 19000 cm^{-1} can be unambiguously assigned[22,31] to the allowed transition to $E_u''(^2T_{2u})$ + $U_u'(^2T_{2u})$ states, where the Ham effect is present,[50,51] and $U_u'(^2T_{1u})$, respectively. In doped crystals, these transitions exhibit the 19500- and 20800-22800 cm^{-1} fine structure attributed to mixing between the U_u' and E_u' components of $^2T_{1u}$ and the orbitally-forbidden transition into $E_u'(^2T_{1u})$, respectively.[22] Because of considerably larger ζ_{Br}, the ligand spin-orbit splittings are observable more readily in the spectrum of $IrBr_6^{2-}$ than $IrCl_6^{2-}$,[20] Table 1 and Fig. S1 in ESI.

3.3 Ultrafast transient absorption

Following 1900-nm excitation of $IrCl_6^{2-}$ into $U_g'(^2T_{2g})$ in acetonitrile, the 100-fs ΔA spectrum shows dual-band ground-state bleach of $IrCl_6^{2-}$ and induced absorption with 654, 542 (intense) and ~600 nm (weaker) bands, Fig. 3a. The 542 and 654 nm ΔA bands, when shifted by the 1900-nm photon energy (which also is the energy gap between U_g' and E_g''), match the positions of the steady-state 492- and 437-nm absorption bands, Fig. S2 of ESI. Therefore, the 100-fs induced absorption is assigned to excited-state absorption (ESA) from the initial, Franck-Condon (FC) $U_g'(^2T_{2g})$ state. The ΔA spectra slowly decay with the isosbestic point at 512 nm and no change in the spectral shape within 2 ns. No ΔA signals are observed after 2 ns, manifesting that all $U_g'(^2T_{2g})$ population completely returned back into the GS. Upon 600-nm excitation into $U_g'(^2T_{1g})$, the initial (0 fs) ΔA spectrum shows the 436- and 488-nm ground state bleach, a broad ~550-700-nm induced absorption, and induced absorption below 400 nm, Fig. 3b. These signals continue to grow within the first 100 fs as the excitation pulse continues to populate the FC state, Fig. 3b and Fig. S3 of ESI. From 100 fs to 1 ps, the broad ~550-700-nm feature undergoes a minor reshaping (decay on the red side and rise on the blue side) forming a broad band with a flat 550-650 nm maximum. From 1 to ~10 ps, the ΔA signals below 400 nm decay, and the 550-650-nm band evolves (isosbestic point, 689 nm) into three pronounced 545-, ~600- and 654-nm bands. Based on the 1900-nm excitation experiment, these bands manifest the population of the $U_g'(^2T_{2g})$ state. After 10 ps, the ΔA spectra decay identically to the 1900-nm excitation case. Excitation at 490 nm

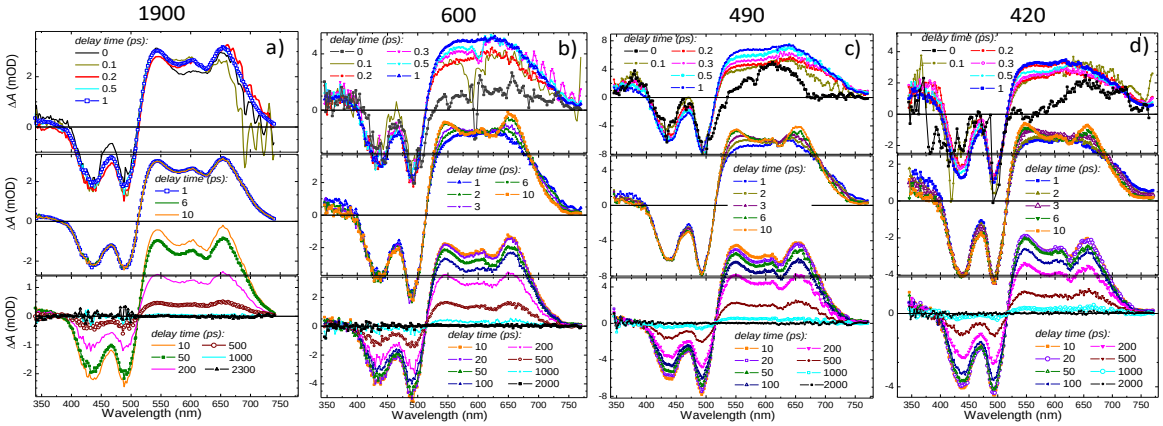

Fig. 3. Transient absorption spectra of $IrCl_6^{2-}$ in acetonitrile excited at 1900 nm (a), 600 nm (b), 490 nm (c), and 420 nm (d). Delay times between the excitation and probe pulses are given in the legends. The ΔA spectra measured at short, intermediate, and long delay times are shown from top to bottom. The 0 and 100 fs ΔA spectra, from which solvent contribution was subtracted (Supporting Information), show small residual solvent oscillatory signals from 675 to 760 nm due to cross-phase modulation, impulsive stimulated Raman scattering (ISRS), and stimulated Raman emission on the Stokes side for 490 nm excitation (an inverted 580 nm spike at 0 fs due to the Raman-active C-H stretching mode at 2942 cm^{-1}).

into $U_u'(^2T_{1u})$ leads (0 fs) to a narrow 625-nm ΔA band, Fig. 3c and Fig. S3 of ESI. A rise of induced absorption between 530 and 590 nm, and above 650 nm, continues up to 200 fs and is accompanied by a very small change in the bleach signals. The ΔA spectrum at 200 fs resembles that observed 100 fs following 600-nm excitation. After 500 fs, the ΔA spectra for these two excitations become quantitatively identical. Upon 420-nm excitation into $U_u'(^2T_{2u})$ + $E_u''(^2T_{2u})$, the 670-nm ΔA band initially emerges, which within the first 100 fs develops into a broader feature resembling the 550-700-nm ΔA signals observed at 100-200 fs after 490-nm excitation, Fig. 3d and Fig. S3 of ESI. Starting from 200 fs, transient absorption changes for 420 and 490 nm excitation are practically identical: formation and complete decay of three characteristic 542, ~600, 654 nm bands (isosbestic point, 689 nm) is followed by the complete bleach recovery (isosbestic point, 512 nm).

In aqueous solutions, the 200 fs ΔA spectrum following 1900 nm excitation shows ground state bleach (485 and ~415 nm peaks) and three pronounced induced absorption bands (~650, 600, and 532 nm), Fig. 4a, which are similar to those observed upon 1900-nm excitation of $IrCl_6^{2-}$ in acetonitrile. Therefore, these ΔA bands can be likewise assigned to ESA from the FC $U_g'(^2T_{2g})$ state. The decay of transient absorption occurs with no spectral change (isosbestic point, 511 nm) similar to acetonitrile, but much faster (within 100 ps). The 600-nm excitation leads to a broad 600-650-nm ΔA band, which builds up during the pulse and, therefore, can be attributed to ESA from the FC $U_g'(^2T_{1g})$ state, Fig. 4b and Fig. S4 of ESI. This band, between 0.5 and 1 ps, decays yielding the same 651, 602, and 532 nm bands as the ones observed upon 1900 nm excitation, and which decay similarly. There are only minor changes in the ground-state bleach signals prior to ~2 ps. Following 490-nm excitation into $U_u'(^2T_{1u})$, Fig. 4c and Fig. S4 of ESI, the initial (0 fs) ~610 nm ΔA band is replaced at 100 fs by a broad ΔA band extending from ~530 to 770 nm, which looks alike the 600-650 nm ΔA band observed immediately after 600 nm excitation. This indicates that at 100 fs the excited population has reached the $U_g'(^2T_{1g})$ state. Between 500 fs and 1 ps, the ~532, 602, and 651 nm bands develop (isosbestic point, 694 nm), suggesting the population of $U_g'(^2T_{2g})$. At longer times, transient absorption decays in the same manner as for 1900 and 600 nm excitation. Upon 420 nm excitation, the initial ΔA band in the red is at ~670 nm, but starting from 200 fs the ΔA spectra are similar and evolve likewise to the case of 490-nm excitation (isosbestic points at 694 and 511 nm, complete ground-state bleach recovery), Fig. 4d and Fig. S4 of ESI. The kinetic ΔA kinetic traces are shown in Fig. 5 and Fig. S5,6 of ESI.

3.4 Coherent Modulations

Short-time ΔA kinetic traces of $IrCl_6^{2-}$, Fig. 6 and Fig. S7-11 and Table S1 of ESI, show damped coherent modulations. In aqueous solutions upon $U_g'(^2T_{1g})$ excitation, they can be assigned to solute impulsive stimulated Raman scattering (ISRS) because the modulation frequencies (156 and 287 cm^{-1}, FFT) are close to the Raman $\nu_5(t_{2g})$ = 160 cm^{-1} and $\nu_2(e_g)$ = 293 cm^{-1} modes of $IrCl_6^{2-}$ (aqueous hydrochloric acid solution[41]), Fig. S7a of ESI. For 490- and 420-nm excitation into $U_u'(^2T_{1u})$ and $U_u'(^2T_{2u})$ + $E_u''(^2T_{2u})$, respectively, Fig. S8 and S9 of ESI, in addition to the ISRS-induced modulations at 156 and 295 cm^{-1}, the modulations also occur at frequencies of 243 and 104 cm^{-1}, which are quite different from $\nu_5(t_{2g})$ and $\nu_2(e_g)$ and other Raman mode of $IrCl_6^{2-}$ ($\nu_1(a_{1g})$ = 345 cm^{-1} [41]). They are pronounced from ~510 to 770 nm, displaying about three-four periods and occurring out-of-phase in the blue and red wings of this spectral region, Fig. S8 and S9 of ESI and Fig. 6. In acetonitrile, 156-164 and 295 cm^{-1} modulations due to impulsive stimulated Raman scattering of $IrCl_6^{2-}$ were observed (Fig. S7, S9, and S10 of ESI for 600, 420, 490-nm excitation, respectively; the Raman-active t_{2g} and e_g modes of $IrCl_6^{2-}$ in acetonitrile have frequencies of 161 and 290 cm^{-1} [40]).

3.5 $IrBr_6^{2-}$, $E_u''(^2T_{2u})$ excitation

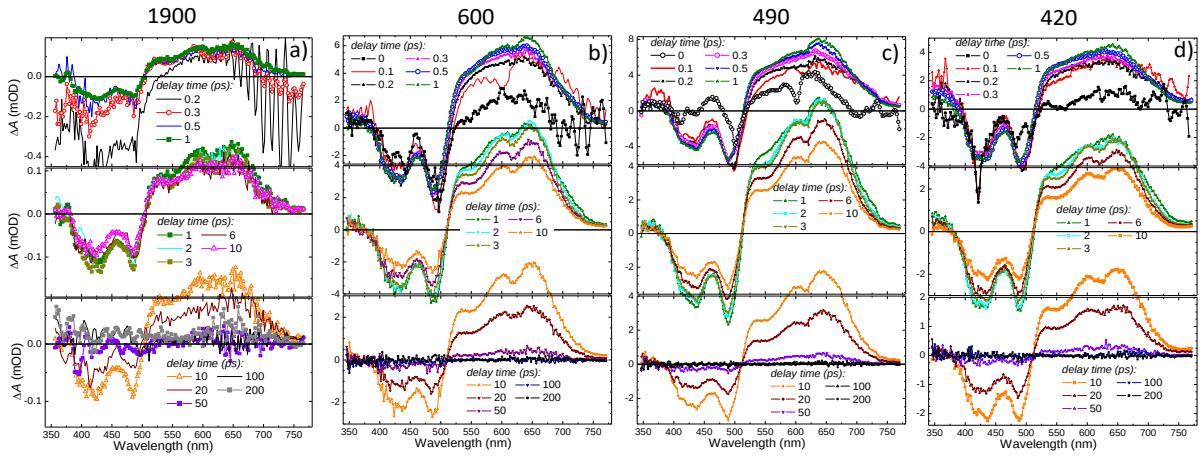

Fig. 4. Transient absorption spectra of $IrCl_6^{2-}$ in aqueous solutions following excitation at 1900 nm (a), 600 nm (b), 490 nm (c), and 420 nm (d). Delay times between the excitation and probe pulses are given in the legends. The ΔA spectra measured at short, intermediate, and long delay times are shown from top to bottom. The 0 and 100 fs ΔA spectra, from which solvent contribution was subtracted (Supporting Information) show some residual solvent oscillatory signals from 675 to 760 nm due to cross-phase modulation, ISRS, and stimulated Raman emission on the Stokes side of the 490 nm excitation (an inverted 600 nm spike at 0 fs due to the Raman-active O-H stretching mode at 3450 cm^{-1}).

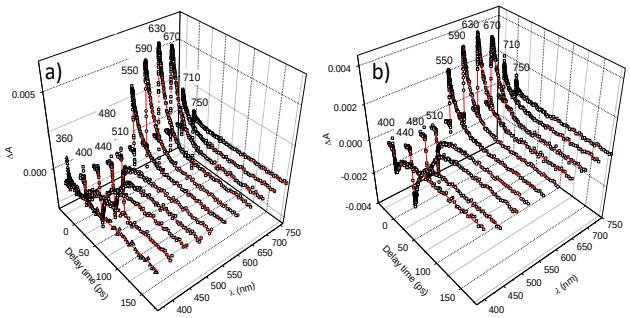

Fig. 5. Representative transient absorption kinetic traces (symbols) of aqueous $IrCl_6^{2-}$ following excitation at 600 nm (a), and 420 nm (b). The probe wavelengths (nm) are shown beside each kinetic trace. Multiexponential fits resulting from the global analysis described in the text are shown as solid red lines. Two-dimensional plots of transient absorption as a function of the time delay for 600-, 490, and 420-nm excitation can be found in Fig. S6 of ESI.

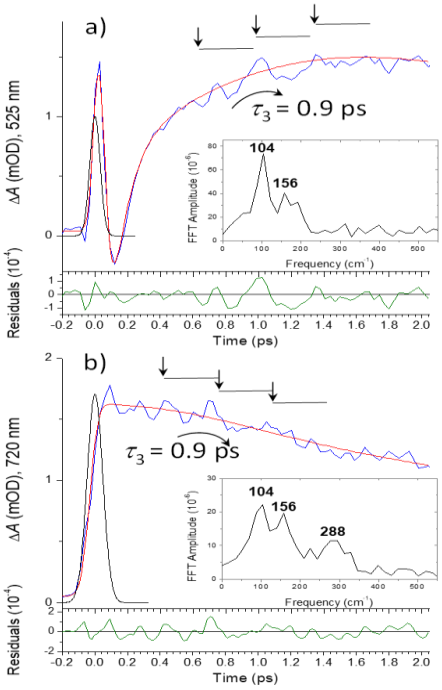

Fig. 6. Transient absorption kinetic traces (blue) at the probe wavelength 525 nm (a) and 720 nm (b), their fits (red) with CCF deconvolution (80 and 100 fs CCF fwhm, respectively; black) and the residual oscillatory components (green) following 420 nm excitation of aqueous $IrCl_6^{2-}$. The horizontal bar represents the period of the 104 cm^{-1} FFT mode (insets). The 525 and 720 nm oscillations are approximately out-of-phase with the apparent beat irregularity caused by the superposition of a 156 and 288 cm^{-1} ISRS-induced ground state wavepacket motion (insets; compare with Raman frequencies, 160 and 290 cm^{-1} [39,41]) and an oscillatory signal coming from water, see also Fig. S9 of ESI for further data. The oscillations are in the $U_g'(^2T_{1g})$ state that is decaying; however, in the 525 nm region absorption from the product state that is being formed predominates, so that the overall signal build up is observed.

Δ*A* spectra of $IrBr_6^{2-}$ in acetonitrile and aqueous solutions following excitation into $U_g'(^2T_{2g})$, $U_g'(^2T_{1g})$, $U_u'(^2T_{1u})$, and $U_u'(^2T_{2u})$ states were reported previously.[64] Herein, we measured Δ*A* spectra following 602-nm excitation of $IrBr_6^{2-}$ into $E_u''(^2T_{2u})$ for comparison with excitation of $IrCl_6^{2-}$ into $E_u''(^2T_{2u})$ + $U_u'(^2T_{2u})$. We found that the relaxation mechanism of $IrBr_6^{2-}$ agrees with the one previously[64] suggested. $U_u'(^2T_{2u})$ states were reported previously.[64] Namely, the 100-fs ~560- and 640-nm Δ*A* bands in acetonitrile (or, the 640-nm Δ*A* band in aqueous solutions, Fig. 7) are similar to $U_u'(^2T_{1u})$ ESA bands,[64] which suggests that $U_u'(^2T_{1u})$ is populated from the FC $E_u''(^2T_{2u})$ state within 100 fs. As manifested by rise (300-500 fs) of the 480-nm band due to $U_g'(^2T_{1g})$ ESA,[64] the $U_u'(^2T_{1u})$ population decays into $U_g'(^2T_{1g})$. Hot complexes in $U_g'(^2T_{1g})$ undergo thermalization, which is seen as narrowing and sub-1 ps shift of the 480-nm band, and populate $U_g'(^2T_{2g})$ on a picosecond timescale. This is demonstrated by the build-up of the characteristic 420- and 740-nm bands corresponding to $U_g'(^2T_{2g})$ ESA.[64,68] $U_g'(^2T_{2g})$ decays completely recovering the ground state population within 2 ns in acetonitrile and 100 ps in water. The 104-121 cm^{-1} oscillations observed are similar in frequency to those previously assigned to the JT-active t_{2g} mode,[64] but are weaker (practically, slightly above the noise level), Fig. S12 of ESI. The 208 cm^{-1} (both in acetonitrile and aqueous solutions) and 173 cm^{-1} (observed in aqueous solution, Fig. S13 and Table S1 of ESI) FFT band are due to vibrational wavepacket motion induced by impulsive stimulated Raman scattering in ground-state $IrBr_6^{2-}$.

3.6 Global fits

The Δ*A* data for $IrCl_6^{2-}$ excited into $U_g'(^2T_{2g})$, $U_g'(^2T_{1g})$, $U_u'(^2T_{1u})$, and $E_u''(^2T_{2u})$ + $U_u'(^2T_{2u})$ can be satisfactorily reproduced using one (ε_4), three ($\varepsilon_{2\text{-}4}$), four ($\varepsilon_{1\text{-}4}$), and again, four EADS (Fig. 8), respectively, where the resulting time constants ($\tau_{1\text{-}4}$) are summarized in Table 2. Representative fits are shown in Fig. 5 and Fig. S5,6 of ESI. Within a given solvent, all ε_2 and τ_2 are found to be comparable and all ε_3 and τ_3 as well as all ε_4 and τ_4 are found to be identical, supporting the consecutive relaxation mechanism (thereafter, τ_j are given on average for different FC states in a given solvent). Moreover, the ε_4 spectra in CH_3CN and H_2O resemble each other. As 1900-nm excitation only populates

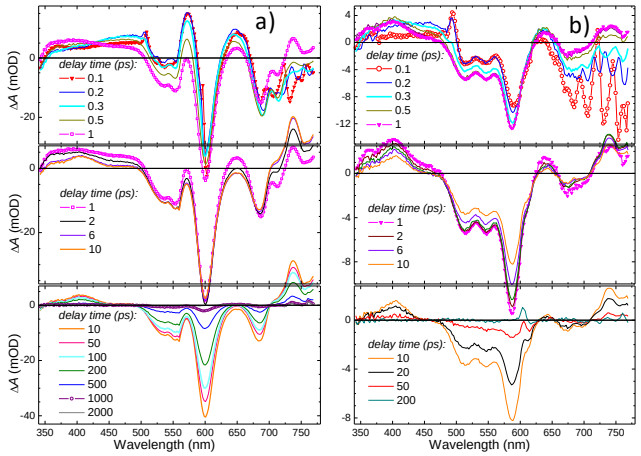

Fig. 7. Transient absorption spectra of $IrBr_6^{2-}$ in acetonitrile (a) and water (b) following excitation at 602 nm into the $E_u''(T_{2u})$ state. The Δ*A* spectra measured at short, intermediate, and long delay times (given in the legends) are shown from top to bottom. In (b), the 685-770 nm region in the short-time 100 and 200 fs Δ*A* spectra shows strong ISRS signals from water. A small 602 nm feature in the long-time Δ*A* spectra (b) is due to the scattered excitation light; transient absorption (a and b) at long times decays to zero.

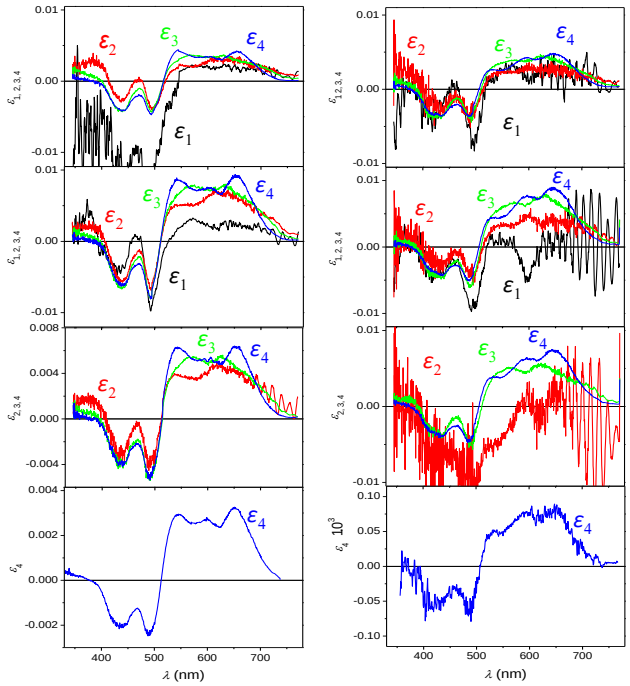

Fig. 8. Evolution-associated difference spectra (ε_j) extracted from the global fit of the ΔA spectra of $IrCl_6^{2-}$ acetonitrile (left) and water (right). Excitation at 420, 490, 600, and 1900 nm (top to bottom).

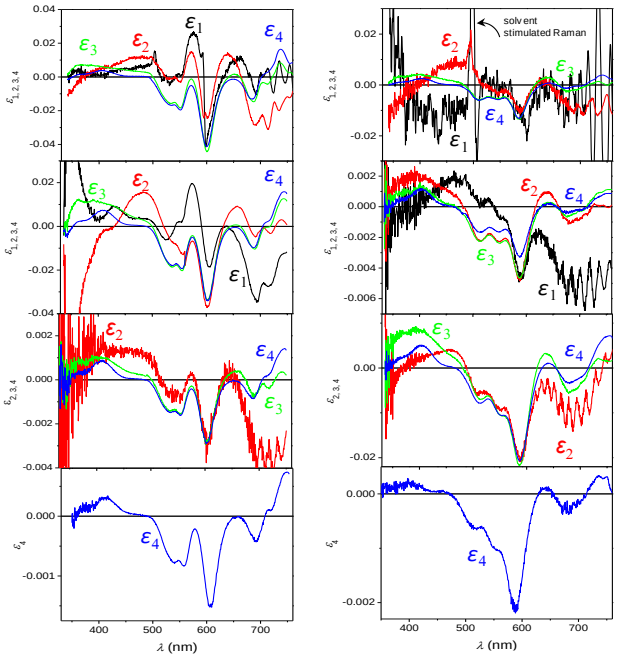

Fig. 9. Evolution-associated difference spectra (εj) extracted from the global fit of the ΔA spectra of $IrBr_6^{2-}$. Left: acetonitrile solutions, excitation at 602, 760, 870, and 2000 nm (top to bottom). Right: aqueous solutions, excitation at 602 nm, 745, 880 and 1880 nm (top to bottom).

$U_g'(^2T_{2g})$, τ_4 is the lifetime of this excited state, and also, the ground-state recovery time constant. The $U_g'(^2T_{2g})$ lifetime is much shorter in H_2O than CH_3CN: 19.3 vs. 370 ps. The first process following $U_g'(^2T_{1g})$ excitation (τ_2, $\varepsilon_2 \rightarrow \varepsilon_3$) is attributed to vibrational relaxation because the ε_2 resembles the subsequent ε_3, but it is broader and red-shifted (above 600 nm). Therefore, all ε_2 and ε_3 correspond to ESA from hot and thermalized $U_g'(^2T_{1g})$, respectively. In CH_3CN and H_2O, τ_2 ~600 and 200 fs, respectively, showing some variation with the excitation wavelength. Solute intramolecular vibrational energy redistribution (IVR) and solute-solvent vibrational energy transfer (VET) typically manifest themselves through narrowing and blue shift of solute absorption. IVR in polyatomic molecules takes place within a few hundred fs.[79] VET is sensitive to the magnitude of solute-solvent electrostatic interactions, occurring on a sub-picosecond time scale for ions in polar solvents.[80,81] Therefore, both IVR and VET may contribute to τ_2. A blue shift of ESA might also be caused by polar solvation.[82] However, a dominant part of solvation response in water and acetonitrile takes place much faster (~ 60 fs[83]) than the τ_2 observed. Thermalized $U_g'(^2T_{1g})$ decays into $U_g'(^2T_{2g})$ ($\varepsilon_3 \rightarrow \varepsilon_4$, τ_3 = 3.55 ps in CH_3CN and 0.9 ps in H_2O). The complex excited into $U_u'(^2T_{1u})$ undergoes internal conversion (τ_1 ~ 100 fs, $\varepsilon_1 \rightarrow \varepsilon_2$) populating hot $U_g'(^2T_{1g})$. From $E_u''(^2T_{2u})$ + $U_u'(^2T_{2u})$, $IrCl_6^{2-}$ also populates hot $U_g'(^2T_{1g})$ with τ_1 ~ 100 fs. The details of this relaxation process remain unresolved and the τ_1 in this case should be viewed as a time scale, rather than a single time constant.

Table 2. Time constants determined from global fit analysis of transient absorption spectra of $IrCl_6^{2-}$ in CH_3CN and H_2O.

solvent	τ_j, (ps) [e]	Franck-Condon Excited State			
		$U_g'(^2T_{2g})$ [a]	$U_g'(^2T_{1g})$ [b]	$U_u'(^2T_{1u})$ [c]	$U_u'(^2T_{2u})$ + $E_u''(^2T_{2u})$ [d]
CH_3CN	τ_1	-	-	0.13±0.03	0.11±0.08
	τ_2	-	0.62±0.03	0.74±0.08	0.51±0.04
	τ_3	-	3.4±0.2	3.5±0.3	3.8±0.3
	τ_4	382±11	366±3	361±12	369±3
H_2O	τ_1	-	-	0.08±0.02	0.08±0.02
	τ_2	-	0.07±0.01	0.20±0.01	0.22±0.02
	τ_3		0.77±0.06	0.98±0.05	0.93±0.17
	τ_4	23.5±2.5	17.7±0.1	17.9±0.1	18.0±0.1

[a] 1900 nm, [b] 600 nm, [c] 490 nm, [d] 420 nm excitation wavelengths; [e] j = 1, 2, 3, and 4 components describe the decay processes $\varepsilon_1 \rightarrow \varepsilon_2$, $\varepsilon_2 \rightarrow \varepsilon_3$, $\varepsilon_3 \rightarrow \varepsilon_4$, and $\varepsilon_4 \rightarrow$ ground state, respectively, see Fig. 8. Errors bars given are those of the global fits of the kinetic data.

We also carried out global analysis of ΔA data for $IrBr_6^{2-}$ measured previously ($U_g'(^2T_{2g})$, $U_g'(^2T_{1g})$, and $U_u'(^2T_{1u})$ excitation)[64] and in this work ($E_u''(^2T_{2u})$ excitation), which required one, three, four, and four sets of EADS, respectively, Fig. 9. The resulting time constants ($\tau_{1\text{-}4}$, Table 3) are found to be similar to those obtained from multiexponential fits of ΔA kinetic traces in the previous work,[64] and therefore they are interpreted in the same manner. In the $E_u''(^2T_{2u})$ case, we simplified the global fit description and approximated the decay of $E_u''(^2T_{2u})$ and the subsequent decay of $U_u'(^2T_{1u})$ using a single τ_1 (~100 fs). The subsequent $\varepsilon_{2\text{-}4}$ and $\tau_{2\text{-}4}$ turned out to be similar to the $\varepsilon_{2\text{-}4}$ and $\tau_{2\text{-}4}$ values obtained for excitation into $U_g'(^2T_{1g})$ and $U_u'(^2T_{1g})$.

Table 3. Time constants determined from global fit analysis of transient absorption spectra of $IrBr_6^{2-}$ in various solvents.

solvent	τ_j (ps) [f]	Franck-Condon Excited State			
		$U_g'(^2T_{2g})$ [a]	$U_g'(^2T_{1g})$ [b]	$U_u'(^2T_{1u})$ [c]	$E_u''(^2T_{2u})$ [d]
CH_3CN [e]	τ_1	-	-	0.088±0.030	0.12±0.07
	τ_2	-	0.23±0.06	0.41±0.07	0.41±0.09
	τ_3	-	2.48±0.25	2.78±0.05	2.6±0.2
	τ_4	323±1	356±19	343±4	325±25 [e]
H_2O	τ_1	-	-	0.101±0.016	0.06±0.03
	τ_2	-	0.18±0.05	0.34±0.03	0.30±0.15
	τ_3	-	0.53±0.15	0.66±0.34	0.7±0.2
	τ_4	20.8±0.8	20.6±0.5	21.5±0.6	21.9±0.1

[a] 2000 nm (CH_3CN) and 1880 nm (H_2O), [b] 870 nm (CH_3CN) and 880 nm (H_2O), [c] 760 nm (CH_3CN) and 745 nm (H_2O), [d] 602 nm (CH_3CN and H_2O) excitation wavelengths, [e] anhydrous acetonitrile, except $^2E_u''(T_{2u})$ excitation where acetonitrile was used as received, [f] j = 1, 2, 3, and 4 components describe the decay processes $\varepsilon_1 \rightarrow \varepsilon_2$, $\varepsilon_2 \rightarrow \varepsilon_3$, $\varepsilon_3 \rightarrow \varepsilon_4$, and $\varepsilon_4 \rightarrow$ ground state, respectively, see Fig. 9. Errors bars given are those of the global fits of the kinetic data.

In all these cases the red-shifted and broader ε_2, in comparison with the ε_3, suggests that the τ_2 describes vibrational relaxation of hot $U_g'(^2T_{1g})$. Thermalized $U_g'(^2T_{1g})$ (ε_3) decays with τ_3 into $U_g'(^2T_{2g})$ (ε_4), which decays with τ_4 into the ground state.

4. Discussion

The low-lying excited states of $IrCl_6^{2-}$ are all LMCT, with the exception of the lowest $U_g'(^2T_{2g})$ state, which is intraconfigurational, Table 1. The energy gap of 23800 cm^{-1} between the ground state and the highest LMCT state investigated in this work spans several excited states, which are (in the order of decreasing energy) $U_u'(^2T_{2u}) + E_u''(^2T_{2u})$, $E_u'(^2T_{1u})$, $U_u'(^2T_{1u})$, $E_g'(^2T_{1g})$, $U_g'(^2T_{1g})$, and $U_g'(^2T_{2g})$, Fig. 10. We observed that $IrCl_6^{2-}$ excited into any of these states, except from $E_u'(^2T_{1u})$ and $E_g'(^2T_{1g})$, which are electric dipole forbidden from the $E_g''(^2T_{2g})$ ground state, undergoes cascade radiationless relaxation back into the ground state. Higher LMCT $U_u'(^2T_{1u})$ and $U_u'(^2T_{2u}) + E_u''(^2T_{2u})$ states decay leading to $U_g'(^2T_{1g})$, populated at ~100 fs. This lowest LMCT state decays (lifetime, 3.55 ps in CH_3CN and a 0.9 ps in H_2O) as the $U_g'(^2T_{2g})$ intraconfigurational state builds up, giving rise to an isosbestic point. No ground state repopulation occurs in this relaxation cascade because the bleach recovery is only observed on a picosecond timescale when the lowest-excited $U_g'(^2T_{2g})$ state begins to decay into the ground state (a 370 ps lifetime in CH_3CN and a 19.3 ps lifetime in H_2O, a rate-limiting step of the entire cascade).

Based on our results, the $E_g''(^2T_{2g}) \rightarrow U_g'(^2T_{2g})$ intraconfigurational transition in room-temperature liquids can be placed either at 5100 cm^{-1} (the maximum of the $E_g'' \rightarrow U_g'$ band, Fig. 1) or 5227 cm^{-1} (given by the best match between the positions of the 437- and 492-nm steady-state transitions in comparison to the 544- and 654-nm $U_g'(^2T_{2g})$ ESA bands, Fig. S2 of ESI). The high-resolution low-temperature spectroscopic studies reported the origins of the $E_g'' \rightarrow U_g'$ transition at 5144 and 5142(7) cm^{-1}.[25,26] One can state that within 100 cm^{-1} the splitting of the U_g' and E_g'' $^2T_{2g}$ states is the same for these different environments. It was challenging to locate $E_u'(^2T_{1u})$ in previous work because absorption from the ground state into this state is forbidden. However, from $U_g'(^2T_{2g})$ it is allowed. The 602-nm (acetonitrile) ESA band is the only possible assignment for the $U_g'(^2T_{2g}) \rightarrow E_u'(^2T_{1u})$ transition because it is intense and located between the 544 and 654 nm ΔA bands corresponding to ESA from $U_g'(^2T_{2g})$ into $U_u'(^2T_{2u}) + E_u''(^2T_{2u})$ and $U_u'(^2T_{1u})$. We thus locate $E_u'(^2T_{1u})$ at 21710 cm^{-1} ($5100 + 10^7/602$) above the ground state. The resonance Raman study of $IrCl_6^{2-}$ in solid films (15 K) located the $E_g''(^2T_{2g}) \rightarrow E_u'(^2T_{1u})$ transition at 21186 cm^{-1}, which is close.[36]

The 104- and 243-cm^{-1} oscillation frequencies observed for aqueous $IrCl_6^{2-}$ following excitation into the $U_u'(^2T_{2u}) + E_u''(^2T_{2u})$ and $U_u'(^2T_{1u})$ states are very different from the frequency of a_{1g} vibration, which typically appears in ultrafast pump-probe measurements,[84,85] as well as that of other two Raman-active modes of ground-state $IrCl_6^{2-}$ (345 cm^{-1} a_{1g}, 293 cm^{-1} e_g, and 160 cm^{-1} t_{2g} [41]). The oscillations exhibit a $\sim\pi$ shift and, therefore, should be assigned to vibrational coherence.[86-88] They become damped as $U_g'(^2T_{1g})$ decays, and therefore, should occur in $U_g'(^2T_{1g})$. $U_u'(^2T_{1u})$ and $U_u'(^2T_{2u}) + E_u''(^2T_{2u})$ populate $U_g'(^2T_{1g})$ on a 100 fs timescale. Population relaxation on this timescale is usually a result of a conical intersection (CI) between the involved potential energy surfaces (PESs).[89]

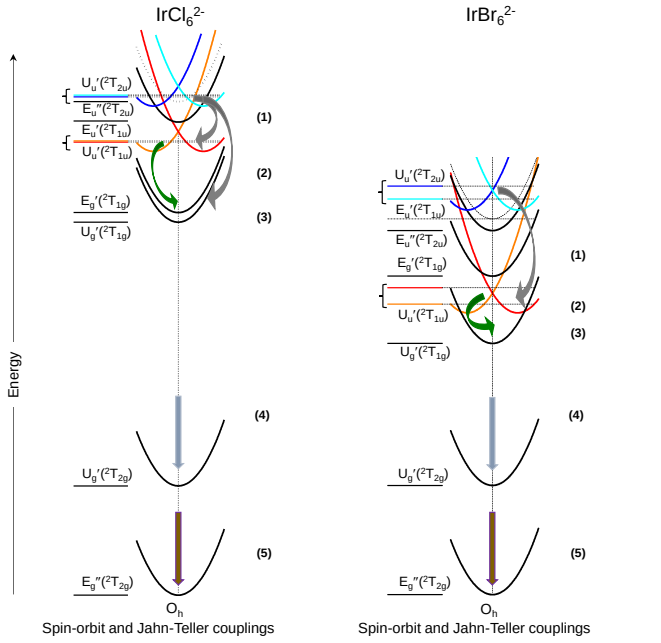

Fig. 10. Cascade radiationless relaxation pathways (1-5) following excitation of O_h $IrCl_6^{2-}$ and $IrBr_6^{2-}$ into U_u' states destabilized by the JT effect. $IrBr_6^{2-}$ excited into any higher LMCT states ($E_u''(^2T_{1u})$ was not studied) undergoes sub-100 fs internal conversion (1) into $U_u'(^2T_{1u})$, which decays (2) into vibrationally coherent $U_g'(^2T_{1g})$ (time constant, ~90 fs). In $IrCl_6^{2-}$, lifetimes of $U_u'(^2T_{2u}) + E_u''(^2T_{2u})$ (superimposed due to Ham effect) and $U_u'(^2T_{1u})$ are also ~100 fs, and $U_g'(^2T_{1g})$ is formed vibrationally coherent, but no definite conclusion can be made regarding the intermediacy of $U_u'(^2T_{1u})$. $IrCl_6^{2-}$ and $IrBr_6^{2-}$ undergo vibrational relaxation in $U_g'(^2T_{1g})$ (process 3, sub-700 fs), picosecond decay into $U_g'(^2T_{2g})$ via back electron transfer (4), and much slower internal conversion from $U_g'(^2T_{2g})$ into the ground $E_g''(^2T_{2g})$ state (5). Time constants of pathways (3-5) are solvent dependent, Table 2 and Table 3.

In d^5 Oh hexahalides, orbital T terms are split by spin-orbit interaction into U' and E'(or, E'') electronic states, where the degenerate U' states correspond to symmetry-determined JT-type CI.[90,91] In these U' states, JT effect is possible. The previous work on $IrCl_6^{2-}$ in low-temperature host lattices[22,31,50,51] provided considerable evidence for the Ham effect (which is quenching of SOC by a dynamic JT effect[92]), which manifestation is a small (5-6 cm^{-1}) splitting of the U_u' and E_u'' $^2T_{2u}$ components, rather than the expected splitting of $3/4\xi_{Cl}$ ~ 440 cm^{-1},[31,50] so that ~420 nm band is practically due to the $U_u'(^2T_{2u})$ + $E_u''(^2T_{2u})$ states. The Ham effect may also be present in $^2T_{1u}$.[31] Other authors questioned the relevance of the Ham effect and invoked low-symmetry static distortion of the lattice as an explanation.[33] There is no observable JT effect in $U_g'(^2T_{2g})$,[25,26,36] which PES is nested and nearly identical relative to the ground state PES, and also, $U_g'(^2T_{1g})$.[31] Since the antisymmetric products of U' yield A_{1g} + E_g + T_{2g},[12] the JT coupling within the vibrational manifold of U' states is possible for triply degenerate bending (t_{2g}), doubly degenerate out-of-phase stretching (e_g), and totally symmetric stretching (a_{1g}) modes, which are also Raman-active,[36,38-40] see Fig. S14 of ESI for schematic representation of the corresponding nuclear motion. The initial acceleration of a wavepacket launched by the impulsive excitation should occur along the nuclear displacements corresponding to the Raman-active modes as they have the steepest slopes in the FC region.[93] Distortions along t_{2g} and e_g remove the initial degeneracy of U_u' states with the horizontal displacement and energetic stabilization of the resulting (diabatic) surfaces, which may lead to electronic curve crossing and ~100 fs population transfer into a lower state (provided that the crossing region from the resulting surface is accessible). Product vibrational coherence may result from curve crossing itself for a strong coupling,[94,95] or be transferred from the FC state. In the aftermath, wavepackets in Raman- JT-active modes move within the product potential well, modulating product absorption. Our observation of the 243-cm^{-1} oscillations upon $U_u'(^2T_{1u})$ excitation are consistent with the JT coupling of this state with the e_g mode, and based on weak ~120 cm^{-1} FFT signals, Fig. S8 of ESI, with some coupling to the t_{2g} mode (t_{2g} and e_g frequencies are always below and above 200 cm^{-1} in O_h hexahalides[50]). The 104 cm^{-1} oscillations observed upon 420-nm excitation are consistent with JT coupling of $U_u'(^2T_{2u})$ + $E_u''(^2T_{2u})$ with t_{2g} proposed in high resolution MCD and spectroscopic studies of Cs_2ZrCl_6 lattices.[22,31,50,51]

Next, we compare the relaxation dynamics studied through seven low-lying excited-states for $IrCl_6^{2-}$ and isoelectronic $IrBr_6^{2-}$. Both complexes have O_h geometry, a ground electronic state of $E_g''(^2T_{2g})$ symmetry and the same nature of the intraconfigurational and LMCT excited states all originating from electron promotion into the same $e_g''(t_{2g})$ predominantly metal orbital considered to be non-bonding (heavy metals)[18,96] in ligand field theory. There are several differences between $IrCl_6^{2-}$ and $IrBr_6^{2-}$. Different LF (t_{2g} and e_g) splitting of the 5*d* orbitals is not relevant to the current work because the $e_g''(t_{2g})$ orbital is much lower than the e_g orbital. Replacement of bromide ligands with chlorides shifts the LMCT band barycenters by ~5000 cm^{-1} to higher energies because of the different reducing strength of these ligands.[22,49] SOC constants are functions of the forth power of an atom's effective nuclear charge and, therefore, much higher for the bromide than chloride ligands (ζ_{Br} = 2457 cm^{-1} > ζ_{Cl} = 587 cm^{-1} [20]). The SOC effects are manifested through a smaller ligand spin-orbit splitting in the chloride spectrum and the different ordering of the LMCT states ($E_u'(^2T_{1u})$ and $E_g'(^2T_{1g})$ are pushed up to higher energy in the bromide), Fig. 2. Besides, large SOC (or, JT effect) can quench JT effect (or, SOC).[15,20,22,50,51]

We found that the chloride and the bromide species follow a similar tier cascade relaxation mechanism. The LMCT states derived from T_{2u}, the highest-energy orbital parentage studied, are all short-lived (≤100 fs); $U_u'(^2T_{2u})$ + $E_u''(^2T_{2u})$ for $IrCl_6^{2-}$ and $U_u'(^2T_{2u})$[64] and $E_u''(^2T_{2u})$ for $IrBr_6^{2-}$, and populate (~100 fs) the lowest-energy LMCT $U_g'(^2T_{1g})$ state. In this process in $IrBr_6^{2-}$, $U_u'(^2T_{1u})$ acts as an intermediate ($U_u'(^2T_{2u})$[64] and $E_u''(^2T_{2u})$, this work). In $IrCl_6^{2-}$, the intermediacy of $U_u'(^2T_{1u})$ is unresolved. Following vibrational relaxation in $U_g'(^2T_{1g})$, the thermalized $IrCl_6^{2-}$ and $IrBr_6^{2-}$ decay into $U_g'(^2T_{1g})$, and subsequently, $U_g'(^2T_{2g})$. These two decay processes resemble each other in the chloride and the bromide, occurring with solvent-dependent time constants ranging from several hundred femtoseconds to a few picoseconds and from several tens to several hundreds of picoseconds, respectively, Table 2 and 3.

For $IrCl_6^{2-}$ and $IrBr_6^{2-}$, we found no vibrational coherence following excitation into $U_g'(^2T_{2g})$, in agreement with the previous studies in cold host crystals, which reported no observable JT effect in this state,[25,26,36] and also, following excitation into $U_g'(^2T_{1g})$. For $IrCl_6^{2-}$ excited into $U_u'(^2T_{1u})$, the vibrational coherence manifests the JT coupling of this state to e_g. The JT effect in $U_u'(^2T_{1u})$ was previously suspected.[31] For $U_u'(^2T_{2u})$ + $E_u''(^2T_{2u})$ excitation, the vibrational coherence observed suggests vibronic mixing that involves t_{2g} and no e_g JT activity, consistent with what was proposed for these excited states on the basis of the large JT and Ham effect.[20,50,51] For $IrBr_6^{2-}$, the cold crystal studies concluded that a large ligand SOC quenched the Ham effect. [31,50,51] There is the JT coupling to t_{2g} and e_g modes in the $U_u'(^2T_{1u})$ state and the JT effect in the $U_u'(^2T_{2u})$ state is weak.[21,22,50] In agreement, in the ultrafast transient absorption study[64] vibrational coherence (observed in $U_g'(^2T_{1g})$ as for $IrCl_6^{2-}$) was more pronounced upon excitation into $U_u'(^2T_{1u})$ than $U_u'(^2T_{2u})$; the frequency (104 cm^{-1} in acetonitrile and 125 cm^{-1} in aqueous solution) closely agreed with that of the t_{2g} mode (~97 cm^{-1} in the ground state[20,37,39,41]). This agreement implies that the shape of the $U_g'(^2T_{1g})$ potential along this nuclear displacement is close to that of the ground state. Overall, these results suggest that the JT models developed for $IrCl_6^{2-}$ and $IrBr_6^{2-}$ in cold host crystals[20,50,51] hold to a large degree when these ions are surrounded by polar solvent at room temperature.

These JT interactions cause ultrafast (100-fs) population dynamics in T_{1u} and T_{2u} states of $IrBr_6^{2-}$ and $IrCl_6^{2-}$, which are at the top of the LMCT manifold of the excited states studied. They all correspond to electron promotion into the same non-bonding $e_g''(t_{2g})$ orbital. As a consequence, at the O_h geometry of the ground state, the ground state, LMCT, and intraconfigurational $U_g'(^2T_{2g})$[25,26,36] potentials are all nested and

weakly coupled. There is no JT effect in $U_g'(^2T_{1g})$ and $U_g'(^2T_{2g})$ and, in addition, these excited states are energetically isolated, and therefore, long-lived for both $IrBr_6^{2-}$ and $IrCl_6^{2-}$. Excitation into E'' and E' states could not be investigated for $IrCl_6^{2-}$. For $IrBr_6^{2-}$ promoted into $E_u''(^2T_{2u})$ (solvent: acetonitrile and water, this work, and chloroform, previous work[64]) and $E_g'(^2T_{1g})$ (chloroform solvent, previous work[64]), the t_{2g} and e_g Raman displacements cause the population to traverse the region of strong coupling between these PESs, which remain nested at O_h (E'' and E' states being the Kramers doublets[12,15] are stable against the JT distortion), and the lower PES of formerly $U_u'(^2T_{1u})$ that underwent JT distortion along t_{2g} and e_g, with sub-100 fs population transfer to the latter surface. Following excitation into the U_u' components of T_{1u} and T_{2u} (both $IrBr_6^{2-}$ and $IrCl_6^{2-}$) initial nuclear displacements along the Raman-active t_{2g} and e_g modes now cause JT distortions of the initial PES, causing the population to traverse the region of strong coupling with a lower PES with sub-100 fs population transfer to the latter. We found this to be another U' PES, whereas population of E'' and E' states is not observed in these experiments. For $IrBr_6^{2-}$, specifically, it is the population transfer from $U_u'(^2T_{2u})$ into $U_u'(^2T_{1u})$ and from $U_u'(^2T_{1u})$ into $U_g'(^2T_{1g})$. For $IrCl_6^{2-}$, $U_g'(^2T_{1g})$ is populated from $U_u'(^2T_{1u})$ as well as $U_u'(^2T_{2u}) + E_u''(^2T_{2u})$ (in the last case, the intermediacy of $U_u'(^2T_{1u})$ is unresolved). For both $IrCl_6^{2-}$ and $IrBr_6^{2-}$, the ~100 fs ESA spectra from $U_g'(^2T_{1g})$ populated either from higher states or by the direct excitation from the O_h ground state resemble each other. This possibly indicates that JT distortions acquired in the course of radiationless relaxation are reverted back in the first excited LMCT state, which is consistent with the complex geometry close to O_h and no reported JT activity in this state.

The Laporte forbidden $E_g''(^2T_{2g}) \rightarrow U_g'(^2T_{1g})$ optical transition borrows intensity from mixing with odd parity modes. The spectral resemblance of the $U_g'(^2T_{1g})$ ESA mentioned above may possibly suggest that in a course of radiationless relaxation from higher LMCT into $U_g'(^2T_{1g})$ vibrational energy is predominantly deposited into the same odd-parity modes. We note that vibrational relaxation in $U_g'(^2T_{1g})$ $IrBr_6^{2-}$ is more pronounced and much less solvent dependent with that in $U_g'(^2T_{1g})$ $IrCl_6^{2-}$ (*cf*. the τ_2 entries in Table 2 and 3; 0.25 ps was reported for vibrational relaxation of $IrBr_6^{2-}$ in $CHCl_3$ [64]). This may indicate a larger relative contribution of IVR than IET in the bromide, because IET is expected to be much more sensitive to electrostatic interactions between solute and solvent and thus much slower in less polar environment.

The radiationless decay $U_g'(^2T_{1g}) \rightarrow U_g'(^2T_{2g})$ represents back electron transfer. The corresponding time constants from global fits (τ_3) are 0.9 and 0.65 ps in water and 3.55 and 2.6 ps in acetonitrile, respectively, for $IrCl_6^{2-}$ and $IrBr_6^{2-}$. For the same process in $IrBr_6^{2-}$, multiexponential fits of representative ΔA kinetic traces in the previous work yielded 2.8 ps[64] (i.e. comparable), and 3 ps (in chloroform) time constants. Several picosecond lifetimes suggest that this process corresponds to the intermediate coupling limit of the gap law (a small displacement of the minima of the upper and lower surfaces).[97] In this case, the rate constant of radiationless decay between two states is $k \propto exp\ (-\Delta E/\hbar\omega)\rho(\omega)$, where $\Delta E/\hbar\omega$ is the number of quanta of the accepting vibrational mode with the energy $\hbar\omega$ required to bridge the electronic energy gap ΔE, and $\rho(\omega)$ is the density of states. The energy gap between the $U_g'(T_{1g})$ and $U_g'(T_{2g})$ states is ~11600 cm^{-1} in $IrCl_6^{2-}$ (~6500 cm^{-1} in $IrBr_6^{2-}$). The complex may be assumed to relax into $U_g'(^2T_{2g})$ by involving the least number of vibrational quanta consistent with energy conservation.[98] The $U_g'(^2T_{2g})$ potential is nearly identical with that of the ground state in $IrCl_6^{2-}$ and $IrBr_6^{2-}$, where the highest energy vibrations (a_{1g}) are 345[40] and 212[39] cm^{-1}, so the $\Delta E/\hbar\omega$ values (33 and 31, respectively), are identical. Under the assumption that that the density of states scales with the highest-frequency vibrational mode involved in the relaxation, the ratio of the rate constant of radiationless decay for $IrCl_6^{2-}$ and $IrBr_6^{2-}$ is within 20% of the ratio of the τ_3 observed (~1.36 in acetonitrile and ~1.42 in water, Table 2 and 3). Therefore, the back electron transfer rate constants can be explained by the energy gap law.

The decay of the intraconfigurational $U_g'(^2T_{2g})$ state is a rate-limiting step in the entire excited-state relaxation dynamics for both $IrCl_6^{2-}$ and $IrBr_6^{2-}$ (τ_4 = 370 ±9 ps and 337 ±6 ps, respectively). The apparent energy gap between the nested[25,26,36] $U_g'(^2T_{2g})$ excited and $E_g''(^2T_{2g})$ ground state potentials is the same (~5100 cm^{-1}) in both complexes and predominantly determined by the metal SOC.[22,49] Radiationless relaxation $U_g'(^2T_{2g}) \rightarrow E_g''(^2T_{2g})$ is then governed by electronic (SOC) factors predominantly determined by the Ir^{4+} metal center, and largely independent of the ligand nature. There is a somewhat larger CT character in the t_{2g} molecular orbitals in $IrBr_6^{2-}$ according to the relativistic scattered wave calculations,[49] which might account for a somewhat faster decay time of the bromide. One would then expect solvent polarity effect on the $U_g'(^2T_{2g})$ lifetime, which however, is in contrast to what is observed; the $U_g'(^2T_{2g})$ lifetime is practically insensitive of the solvent polarity (346 ± 55 ps in chloroform[64]). A significant shortening of the $U_g'(^2T_{2g})$ lifetime of $IrCl_6^{2-}$ in water is likely to be due to the same energy transfer mechanism proposed for $IrBr_6^{2-}$ that involves OH stretching and bending vibrations,[64] as the bromide and the chloride have the same nature of the $U_g'(^2T_{2g})$ state and the same energy gap separating $U_g'(^2T_{2g})$ from the ground state, and show the same size of the effect (τ_4 = 21.2 ±0.61 ps *vs*. 19.3 ±2.8 ps, Table 2 and 3).

Lastly, the lack of photosubstitution observed for both $IrCl_6^{2-}$ and $IrBr_6^{2-}$ excited up to the T_{2u} LMCT term in acetonitrile and aqueous solutions is consistent with previous studies.[35,60-62,64-67] This term and lower LMCT states all result from electron promotion into the molecular orbital, which predominantly is a t_{2g} 5*d* metal orbital.[49] In addition to a well-known consideration that a t_{2g} 5*d* orbital is fairly inert towards ligand loss (in contrast to an e_g type orbital),[63,99] the current work shows that negligible photochemistry of these complexes upon such excitation is also determined by their dynamics. Sub-100 fs relaxation through LMCT states leads to the lowest LMCT state with a few picosecond lifetime; any photochemistry should occur faster in order to be able to compete. The lowest LMCT state decays into the lowest-excited intraconfigurational state situated at energy too low for a photochemical change. It is also instructive to compare $IrCl_6^{2-}$ and $IrBr_6^{2-}$ to $5d^6$ O_h complexes. There, the three

t_{2g} orbitals are fully occupied. Therefore, all LF (the configuration $t_{2g}^5e_g^1$) and LMCT low-energy excited states must result from electron promotion into an e_g orbital, which has antibonding character with respect to metal-ligand sigma bonds. A reaction characteristic of either of these excited states is loss of a coordinated ligand. $PtBr_6^{2-}$ [100] and $PtCl_6^{2-}$ [67] in aqueous solutions serve as examples.

5. Conclusions

Ultrafast radiationless relaxation dynamics is studied in acetonitrile and aqueous solutions of $IrCl_6^{2-}$, which is isoelectronic to low-spin $3d^5$ compounds, following selective excitation of the complex into low-energy intraconfigurational and three LMCT states spanning the 1900-420 nm energy range. The dynamics is compared to that of isoelectronic $IrBr_6^{2-}$; the excited states in these two octahedra similarly arise from electron promotion into a single vacancy in the e_g'' upper orbital within the LF-induced t_{2g} manifold of the d-shell. Both excited complexes relax via a similar relaxation cascade in which higher ($U_u'(^2T_{2u})$, $E_u''(^2T_{2u})$) and lower ($U_u'(^2T_{1u})$) LMCT states populate in ~100 fs the first LMCT $U_g'(^2T_{1g})$ state. Vibrationally coherence in $U_g'(^2T_{1g})$ suggests that the initial excited-state dynamics is triggered by Jahn-Teller effect. The $U_g'(^2T_{1g})$ state of $IrCl_6^{2-}$, which was unidentified by the previous studies,[65-67] and that of $IrBr_6^{2-}$, also missed in the previous work, [35] subsequently decay into the lowest excited $U_g'(^2T_{2g})$ intraconfigurational state via back electron transfer, which can be characterized by solvent-dependent lifetimes of 3.55 ps ($IrCl_6^{2-}$) and 2.6 ps ($IrBr_6^{2-}$) in acetonitrile and 0.9 ps ($IrCl_6^{2-}$) and 0.65 ps ($IrBr_6^{2-}$) in water, where the difference between the chloride and the bromide is explainable by the energy gap law. The $U_g'(^2T_{2g})$ state, which is 5100 cm^{-1} above the electronic ground $E_g''(^2T_{2g})$ state in both complexes determined by the Ir^{4+} metal center SOC, decays (acetonitrile) into the $E_g''(^2T_{2g})$ with a lifetime of 370 $\pm$ 9 ps for $IrCl_6^{2-}$ and 337 $\pm$ 16 ps for $IrBr_6^{2-}$, i.e., largely independent of the ligand nature. This observation is of special interest in view of $IrCl_6^{2-}$ and $IrBr_6^{2-}$ being isoelectronic to IrF_6^{2-}, which is isoelectronic with comparable chemical and physical characteristics to the IrO_6^{8-} ion, a building block of oxido-iridate materials.[42] The decay of $U_g'(^2T_{2g})$ occurs faster (time constant, ~19 ps) in aqueous solutions due to energy transfer to solvent.

Overall, the results of the current work are important for understanding ultrafast excited-state and charge-transfer (in particular, LMCT) dynamics of high-symmetry complexes of heavier transition metals with significant relativistic contributions as well as the underlying solvent effects. Elucidation of the detail of excited-state JT dynamics has been achieved so far in a handful of coordination compounds,[84,85,100-105] and now in $IrCl_6^{2-}$ and $IrBr_6^{2-}$ d^5 heavy metal complexes. Our results suggest that it is the excited-state Jahn-Teller effect that drives the ultrafast (≤100 fs) relaxation dynamics in d^5 heavy transition metal complexes, rather than spin-orbit effects, which nevertheless are very large in these molecules. We propose that a motion in LMCT excited states along Raman-active modes (a_{1g}, e_g, and t_{2g}) causes a series of conical intersections due to Jahn-Teller distortions in the U_u' LMCT states where these Raman modes are also Jahn-Teller active. For $IrCl_6^{2-}$, the coherent vibrational wavepackets detected suggest that the structural change that facilitates motion through conical intersections is a e_g bending upon excitation into the $U_u'(^2T_{1u})$ state and a t_{2g} torsion upon excitation into the $U_u'(^2T_{2u})$ + $E_u''(^2T_{2u})$ state. Following photoexcitation into the $U_u'(^2T_{1u})$ and $U_u'(^2T_{2u})$ states, a t_{2g} torsional motion facilitates the dynamics through the Jahn-Teller conical intersections for $IrBr_6^{2-}$, driving the initial ~100 fs decay.[64] For $IrBr_6^{2-}$, a series of conical intersections, which are born off and connected by a torsional motion, is essentially the mechanism recently proposed,[35] but in contrast with ref. [35] the motion through this series of conical intersections is initiated by excited-state Jahn-Teller effect instead of spin-orbit coupling driven, and the $U_g'(^2T_{2g})$ intraconfigurational lowest excited state is not connected to any of the LMCT states by accessible conical intersections. Spin-orbit interactions are important as they separate the states vertically, defining the zero-point energy difference between spin-orbit states, but they do not cause electronic curve crossing. On the other hand, Jahn-Teller effect in the excited state leads to a spontaneous (on the time scale of motion along Raman and Jahn-Teller active vibrational modes) symmetry breaking, causing the displacement of the excited state potential and its crossing with other potentials. This, in its turn, triggers the energy and/or charge migration, which may be utilized in molecule-based light-harvesting devices.

Conflicts of interest

There are no conflicts to declare.

Acknowledgements

This work was supported by the NSF (CHE-0847707, DMR-1006761, and CHE-1626420) and BGSU "Building Strength" grants. SMM and DSB gratefully acknowledge McMaster Fellowship. We thank Prof. Mikhail Zamkov (BGSU) for the use of a PerkinElmer spectrometer, and Nicholas Brock-Kyser for assistance in editing and commentary on the manuscript.

References

1 D. M. Roundhill and J. P. Fackler, *Optoelectronic Properties of Inorganic Compounds*, Springer, 1999.
2 R. C. Evans, P. Douglas and H. D. Burrow, *Applied Photochemistry*, Springer, 2013.
3 M. Wermuth and H. U. Güdel, *Chem. Phys. Lett.,* 1997, **281**, 81.
4 D. R. Gamelin and H. U. Güdel, *J. Luminesc.,* 2001, **214**, 1.
5 M. Wermuth and H. U. Güdel, *J. Luminesc.,* 2000, **87-89**, 1014.
6 A.K. Gupta, R. Z. Parker, C. E. Keefer and R. J. Hanrahan, *Solar Energy,* 1993, **51**, 409.
7 A. K. Gupta, R. Z. Parker and R. J. Hanrahan, *Int. J. Hydrogen Energy,* 1993, **18**, 713.
8 H. B. Gray and A. W. Maverick, *Science*, 1981, **214**, 1201.
9 J. G. Rau, E. K. Lee, and H. Y. Kee, Annu. *Rev. Condens. Matter Phys*., 2016, **7**, 195.

10 W. W. Krempa, G. Chen, Y. B. Kim, and L. Balents, Annu. *Rev. Condens. Matter Phys*., 2014, **5**, 57.
11 H. A. Jahn and E. Teller, *Proc. R. Soc. A*, 1937, **161**, 220.
12 H. A. Jahn *Proc. Roy. Soc. A,* 1938, **164**, 117.
13 I. B. Bersuker, *The Jahn-Teller Effect*, Cambridge University Press, Cambridge, 2006.
14 J. S. Griffith, *The Theory of Transition-Metal Ions,* Cambridge University Press, Cambridge, 1961.
15 T. A. Barkholtz and T. A. Miller, *Inter. Rev. Phys. Chem*., 1998, **17**, 435.
16 T. J. Penfold, E. Gindensperger, C. Daniel, and C. M. Marian, *Chem. Rev.,* 2018, **118**, 6975.
17 J. Eng, C. Gourlaouen, E. Gindensperger and C. Daniel, *Acc. Chem. Res.,* 2015, **48**, 809.
18 C. K. Jorgensen, Mol. Phys., 1959, **2**, 309.
19 C. K. Jorgensen, *Progr. Inorg. Chem.,* 1970, **12**, 101.
20 J. R. Piepho, T. E. Lester, A. J. McCaffery, J. R. Dickinson, and P. N. Schatz, *Mol. Phys.,* 1979, **19**, 781.
21 J. R. Dickinson, S. B. Piepho, J. A. Spencer, and P. N. Schatz, *J. Chem. Phys*., 1972, **56**, 2668.
22 P. N. Schatz, in *Electronic States of Inorganic Compounds*, ed. B. P. Day, D. Reidel Publishing Company, Dordrecht, Holland 1975, Vol 20, pp. 223.
23 G. N. Henning, A. J. McCaffery, P. N. Schatz and P. J. Stephens, *J. Chem. Phys.*, 1968, **48**, 5656.
24 I. N. Douglas, *J. Chem. Phys.* 1969, **51**, 3066.
25 T. A. Keiderling, P. J. Stephens, S. B. Piepho, J. L. Slater, and P. N. Schatz, *Chem. Phys.,* 1975, **11**, 343.
26 C. D. Flint and A. G. Paulitz, *Inorg. Chem.*, 1981, **20**, 1768.
27 B. D. Bird, P. Day, and E. A. Grant, *J. Chem. Soc.*, 1970, **100**, 100.
28 G. C. Allen, R. Al-Mobarak, G. A. M. El-Sharkawy, and K. D. Warren, *Inorg. Chem., **11***, 1972, 787.
29 A. J. McCaffery, J. R. Dickinson, and P. N. Schatz, *Inorg. Chem.*, 1970, **9**, 1563.
30 T. P. Sleight and C. R. Hare, *J. Phys. Chem.,* 1968, 72, 2207.
31 S.B. Piepho, J. R. Dickinson, J.A. Spencer, and P. N. Schatz, *J. Chem. Phys.,* 1972, **57**, 982.
32 A. J. McCaffery, P. N. Schatz and T. E. Lester, *J. Chem. Phys.,* 1969, **50**, 379.
33 A. J. McCaffery, M. D. Rowe and D. A. Rice, *J. Chem. Soc. Dalton Trans.,* 1973, 1605.
34 H. Renner, G. Schlamp, I. Kleinwächter, E. Drost, H. M. Lüschow, P.; Tews, P. Panster, M. Diehl, J. Lang, T. Kreuzer, A. Knödler, K. A. Starz, K. Dermann, J. Rothaut, R. Drieselmann, C. Peter, R. Schiele, J. Coombes, M. Hosford and D. F. Lupton, *Platinum group metals and compounds*, In Ullmann's Encyclopedia of Industrial Chemistry, Wiley, 2018, 1.
35 W. P. Carbery, A. Verma, and D. B. Turner, *J. Phys. Chem. Lett*., 8, 2017, 1315.
36 H. Hamaguchi and M. Tasumi, *J. Chem. Phys.,* 1983, **78**, 131.
37 R. J. H. Clark and P. C. Turtle, J. Chem. Soc. Faraday Trans., *1978*, **2**, 74, 2063.
38 H. Hamaguchi, *J. Chem. Phys.,* 1978, **69**, 569.
39 H. Hamaguchi and T.Shimanouchi, *Chem. Phys. Lett.,* 1976, **38**, 370.
40 H. Hamaguchi and T.Shimanouchi, *Chem. Phys. Lett.,* 1975, **32**, 103.
41 Y. M. Bosworth and R. J. H. Clark, *J. Chem. Soc. Dalton Trans*., *1974*, **5**, 1749.
42 K. S. Pedersen, J. Bendix, A. Tressaud, E. Durand, H. Weihe, Z. Salman, T. J. Morsing, D. N. Woodruff, Y. Lan, W. Wernsdorfer, C. Mathonière, S. Piligkos, S. I. Klokishner, S. Ostrovsky, K. Ollefs, F. Wilhelm, A. Rogalev & R. Clérac, *Nat Commun*., 2016, 7, doi:10.1038/ncomms12195
43 M. Kotani *J. Phys. Soc. Japan.,* 1949, **4**, 293.
44 D. N. Figgis, J. Lewis, R. S. Nyholm and R. D. Peacock, *Disc. Faraday Soc.,* 1958, **26**, 103.
45 B. N. Figgis, *Trans. Faraday Soc.,* 1961, **57**, 204.
46 H. Chermette, A. Pertosa, A. Goursot and E. Penigault, *Intern. J. Quant. Chem.,* 1983, **23**, 459.
47 A. Goursot H. Chermette, and C. Daul, *Inorg. Chem.,* 1984, **23**, 305.
48 A. Goursot and H. Chermette, *Chem. Phys*., 1982, **69**, 329.
49 J. P. Lopez and D. A. Case, *J. Chem. Phys*., 1984, **81**, 4554.
50 W. C. Yeakel and P. N. Schatz, *J. Chem. Phys.,* 1974, **61**, 441.
51 W. C. Yeakel, J. L. Slater and P. N. Schatz, *J. Chem. Phys.,* 1974, **61**, 4868.
52 W. Zhang, M. Ji, Z. Sun and K. J. Gaffney, *J. Am. Chem. Soc.,* 2012, **134**, 2581.
53 J. Ojeda, C. A. Arrell, L. Longetti, M. Chergui, and J. Helbing, *Phys. Chem. Chem. Phys.,*
54 B. Bleaney and M. C. M O'Brien, *Proc. Phys. Soc. B* 1956, **69**, 1216-1230.
55 X.-B. Wang and L.-S. Wang, *J. Chem. Phys*., 1999, **111**, 4497.
56 J. Friedrich, S. Glib, O. T. Ehrler, A. Behrendt, and M .M. Kappes, *J. Chem. Phys*., 2002, **117**, 2635.
57 W. E. Boxford, J. K. Pearce, and C. E. H. Dessent, *Chem. Phys. Lett*., 2004, **399**, 465.
58 J. C. Marcum and J. M. Weber, J. Chem. Phys., *2009*, **131**, 194309.
59 C. Rensing, O. T. Ehrler, J. P. Yang, A. N. Unterreiner, and M. M. Kappes, *J. Chem. Phys*., 2009, **130**, 234306.
60 T. P. Sleight and C. R. Hare, *Inorg. Nucl. Chem. Lett*. 1968, **4**, 165.
61 Moggi, G. Varani, M. F. Manfrin and V. Balzani, *Inorg. Chem. Acta*., 1970, **4**, 335.
62 P. K. Eidem, A. W. Maverick and H. B. Gray *Inorg. Chem. Acta.,* 1981, **50**, 59.
63 P. C. Ford, J. D. Petersen and R. E. Hintze, *Coord. Chem. Rev.,* 1974, **14**, 67.
64 S. M. Matveev. D. S. Budkina, I. L. Zheldakov, M. R. Phelan, C. M. Hicks and A. N. Tarnovsky, *J. Chem. Phys*., 2019, **150**, 054302.
65 A. V. Litke, I. P. Pozdnyakov, E. M. Glebov, V. F. Plyusnin, N. V. Tkachenko, and H. Lemmetyinen, *Chem. Phys. Lett*., 2009, **477**, 304.
66 E. M. Glebov, A. V. Kolomeets, I. P. Pozdnyakov, V. F. Plyusnin, N. V. Tkachenko, and H. Lemmetyinen, *Photochem. Photobiol. Sci*., 2001, **10**, 1709.
67 E. M. Glebov, I. P. Pozdnyakov, V. F. Plyusnin, and I. Khmelinskii, *J. Photochem. Photobiol*., 2015, **24**, 1.
68 S. M. Matveev, A. M. Mereshchenko, M. S. Panov, and A. N. Tarnovsky, *J. Phys. Chem. B,* 2015*,* **119**, 4857.
69 S. K. Pal, A. S. Mereshchenko, E. V. Butaeva, P. Z. El-Khoury, and A. N. Tarnovsky, *J. Chem. Phys.*, 2013, **138**, 124501.
70 M. S. Panov, V. D. Voskresenska, M. N. Ryazantsev, A. N. Tarnovsky, and R. M. Wilson, *J. Am. Chem. Soc.*, 2013, **135**, 19167.
71 S. A. Kovalenko, N. Ernsting and J. Ruthmann, *Chem. Phys. Lett*. 1996, **258**, 445-454.
72 S. A. Kovalenko, A. L. Dobryakov, J. Ruthmann, and N. P. Ernsting, *Phys. Rev*., 1999, A **59**, 2369.
73 H. M. van Stokkum, D. S. Larsen and R. van Grondelle, *Biochim. Biophys. Acta, Bioenerg*., 2004, **1657**, 82.
74 C. K. Jorgensen, *J. Inorg. Nucl. Chem.,* 1962, **24**, 1587.
75 D. A. Fine, *Inorg. Chem*., 1969, **8**, 1014.
76 J. M. P. Cabral, *J. Inorg. Nucl. Chem.,* 1964, **26**, 1657.
77 R. F. Fenske, J. Am. Chem. Soc., *1967*, **89**, 252.
78 H.-H. Schmidtke and N. Lehnert, *Inorg. Chem.,* 1988, **37**, 6373.
79 T. Elsaesser and W. Kaiser, *Annu. Rev. Phys. Chem*., 1991, **42**, 83.
80 R. M. Whitnell, K. R. Wilson and J. T. Hynes *J. Phys. Chem.,* 1990, **94**, 8625.
81 I. Benjamin, P. F. Barbara, B. J. Gertner and J. T. Hynes *J. Phys. Chem.,* 1995, **99**, 7557.

82 P. F. Barbara and W. Jarzeba,, in *Adv. Photochem*., ed. B. D. H. Volman, G. S. Hammond and K. Gollnick, John Wiley & Sons, Inc., Hoboken, NJ, USA, 1990, pp. 1.
83 M. L. Horng, J. A. Gardecki, A. Papazyan and M. Maroncelli, *J. Phys. Chem*., 1995, **99**, 17311.
84 D. M. Jonas, *Annu. Rev. Phys. Chem.* 2018, **69**, 327.
85 M. Iwamura, H. Watanabe, K. Ishii, S. Takeuchi and T. Tahara, *J. Am. Chem. Soc.,* 2011, **133**, 7728.
86 D. M. Jonas, S. E. Bradforth, S.A. Passino and G.R. Fleming, *J. Phys. Chem.,* 1995, 99, 2594.
87 M. H. Vos, M. R. Jones and J.-L. Martin, *Chem. Phys*., 1998, **233**, 179.
88 A. T. N. Kumar, F. Rosca, A. Widom, and P. M. Champion, *J. Chem. Phys.,* 2001, **114**,
89 D. Polli, P. Altoè, O. Weingart, K. M. Spillane, C. Manzoni, D. Brida, G. Tomasello, G. Orlandi, P. Kukura, R. A. Mathies, M. Garavelli, and G. Cerullo, *Nature*, 2010, **467**, 440.
90 G. A. Worth and L. S. Cederbaum, *Annu. Rev. Phys. Chem*., 2004, **55**, 127.
91 M. J. Paterson, M. J. Bearpark, M. A. Robb, L. Blancafort and G. A. Worth, *Phys. Chem. Chem. Phys.,* 2005, **7**, 2100.
92 F. S. Ham, *Phys. Rev. A*, 1965, **138**, 1727.
93 E. J. Heller, *Acc. Chem. Res*., 1981, **14**, 368.
94 J. M. Jean and G. R. Fleming, *J. Chem. Phys*., 1995, **103**, 2092.
95 S. Sorgues, J. M. Mestdagh, J. P. Visticot, and B. Soep, *Phys. Rev. Lett*., 2003, **91**, 103001.
96 Y. Jean, *Molecular Orbitals of Transition Metal Complexes*, Oxford University Press, New York, 2005.
97 R. Englman and J. Jortner, *Mol. Phys*., 1970, **18**, 145.
98 V. M. Kenkre, A. Tokmakoff and M. D. Fayer, *J. Chem. Phys*., 1994, 101, 10618.
99 P. S. Wagenknecht and P. C. Ford, Coord. *Chem. Rev*., 2011, **255**, 591.
100 I. L. Zheldakov, M. N. Ryazantsev and A. N. Tarnovsky *J. Phys. Chem. Lett.,* 2011, **2**, 1540.
101 M. Iwamura, S. Takeuchi and T. Tahara, *J. Am. Chem. Soc.,* 2007, **129**, 5428.
102 L. Hua, M. Iwamura, S. Takeuchi and T. Tahara, *Phys. Chem. Chem. Phys*., 2015, **17**, 2067.
103 S. A. Trushin, W. Fuss, W. E.Schmid and K. L. Kompa, *J. Phys. Chem. A,* 1998, **102**, 4129.
104 S. A. Trushin, K. Kosma, W. Fuss and W. E. Schmid, *Chem. Phys.,* 2008, **347**, 309.
105 D. A. Farrow, W. Qian, E. R. Smith, A. A.Ferro and D. M. Jonas, *J. Chem. Phys.,* 2008, **128**, 144510.